Nauschütt *et al. EPJ Techniques and Instrumentation* (2021) 8:13
https://doi.org/10.1140/epjti/s40485-021-00070-x

EPJ Techniques and Instrumentation

RESEARCH ARTICLE Open Access

Non-invasive assessment of plasma parameters inside an ion thruster combining optical emission spectroscopy and principal component analysis

Benny T. Nauschütt*, Limei Chen, Kristof Holste and Peter J. Klar

*Correspondence:
Benny.Nauschuett@physik.uni-giessen.de
Institute of Experimental Physics I, Justus Liebig University, Heinrich-Buff-Ring 16, 35392 Giessen, Germany

Abstract

We present a non-invasive approach for determining plasma parameters such as electron temperature and density inside a radio-frequency ion thruster (RIT) using optical emission spectroscopy (OES) in conjunction with principal component analysis (PCA). Instead of relying on a theoretical microscopic model of the plasma emission to extract plasma parameters from the OES, an empirical correlation is established on the basis of conducting simultaneous OES and Langmuir diagnostics. The measured reference spectra are simplified and a PCA is performed. The PCA results are correlated with the plasma parameters of the Langmuir measurements yielding a one-to-one correspondence. This correlation allows us to derive the plasma parameters by analysis of a non-invasively determined emission spectrum without additional Langmuir measurements. We show how the plasma parameters can be calculated from OES measurements using this correlation. Under the assumption that the electronic system thermalizes on much shorter time scales than the period of the RF signal driving the thruster, we can also use time-resolved spectral data to determine the time evolution of plasma parameters. In future, this method may contribute to shorter test and qualification times of RITs and other ion thrusters.

Keywords: Optical emission spectroscopy, Plasma parameters, Principal component analysis

Introduction

Electric propulsion (EP) systems are nowadays commonly used on spacecrafts [1, 2]. Due to their high thrust to fuel consumption ratio as well as their large variety of different implementations and usable propellants, EP systems are a versatile alternative to their chemical counterparts in many in-orbit applications. One type of EP system is the radio-frequency ion thruster (RIT), which was developed at the Justus Liebig University of Giessen in the 1960s [3, 4]. Inside a RIT, a plasma of the propellant is sustained by inductive heating of its electrons. Positive ions (usually xenon) are accelerated by a system of

extraction grids and expelled from the thruster, thus generating thrust according to Newton's third law [1, 2, 5]. The plasma in the discharge vessel is responsible for the thruster's performance. Thus, knowledge of plasma parameters (e. g., electron temperature and density) may give valuable insight into the erosion processes inside the plasma vessel and of the grid system, but also thruster performance in general. Usually, plasma parameters are determined using invasive electrical probes [6, 7]. For a RIT or other thrusters during qualification for space , it is not desirable to use invasive probes inside the plasma vessel, as they affect the thruster's performance [6] and, if installed permanently, will constitute an additional possible source of failure.

In this paper a method is introduced that utilizes non-invasive optical emission spectroscopy (OES) to assess plasma parameters of an operating thruster. It may be used during terrestrial testing in the context of the qualification process for space. Depending on the thruster, an optical probe can even be installed outside of the ion plume, so plume and probe do not affect each other. Usually, assessing plasma parameters by OES requires complex theoretical modeling of the electronic states of the atoms and ions of the plasma and, via the scattering and recombination processes, their occupation and the optical transitions contributing to the emission spectrum in order to derive a theoretical spectrum which may be compared with experiment.

To circumvent the involved challenges, we pursue an empirical approach which avoids entirely the use of a microscopic plasma model for extracting the plasma parameters from an optical emission spectrum. We measure emission spectra simultaneously with the plasma parameters in a RIT like setup and correlate the results with the help of a principal component analysis (PCA)[8]. This correlation can then be used to determine the state of a plasma non-invasively by simply acquiring an optical emission spectrum and employing the established correlation as long as the plasma is operated in the same range of plasma parameters as used for the reference data set. Ultimately, the method shall be applied to thrusters such as RITs to give an easy and uncomplicated access to plasma parameters and contribute to shorter test cycles and qualification times. It might also be used to optimize a RIT to, for instance, reduce its extraction grid erosion, which partially depends on the plasma parameters and limits its lifetime [9, 10]. Operation of the RIT with low mass efficiency results in a low ionization degree of the plasma and causes more charge exchange reactions, leading to increased sputtering of the acceleration grid. High mass efficient operation, on the other hand, causes a higher electron temperature, which may lead to sputtering on the screen grid.

In case of an RF-plasma, the excitation as well as the plasma parameters and OES are not constant but oscillating in time [11–14]. To examine the time-dependent plasma parameters, time- or phase-resolved spectra can be measured and evaluated using the found correlation.

A brief description of a typical theoretical model is given in "Theoretical and empirical model" section together with a comparison to our approach. The experimental details are described in "Experimental details and theory" section, in particular, the Langmuir and OES measurements as well as the PCA approach correlating the two measurements are explained. The resulting correlation, its application to time-resolved spectra and a corresponding discussion are given in "Results and discussion" section. The paper is concluded in "Conclusion" section where the method is rated and an outlook on future applications is given.

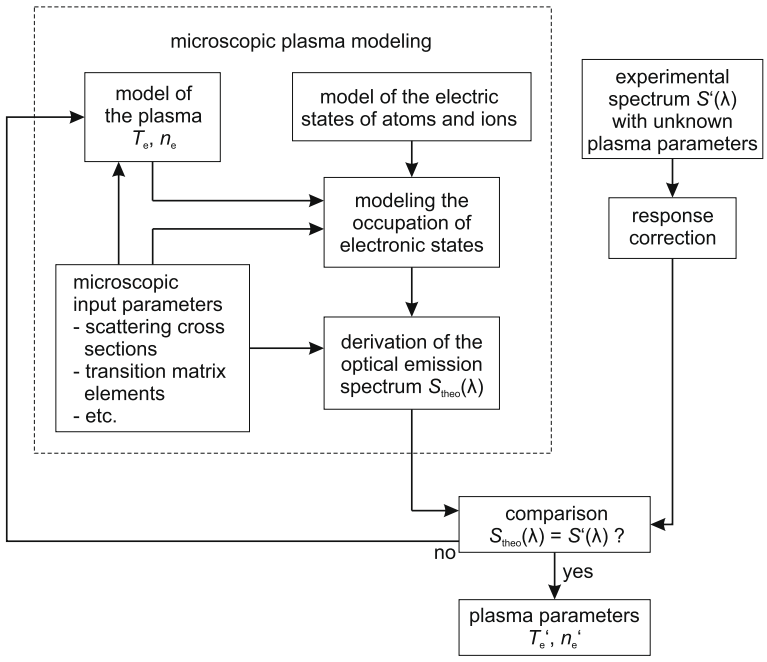

Fig. 1 Schematic description of the work flow necessary to extract plasma parameters from an experimental optical emission spectrum $S'(\lambda)$ by comparison with microscopic theory. The theoretical model contains a microscopic description of the plasma as well as of the electronic states of its ions and atoms. The occupation of these states needs to be modeled based on the microscopic processes inside the plasma. The intensities of the optical transitions need to be calculated based on the occupation of the electronic states and the transition matrix elements in order to obtain a theoretical spectrum $S_{theo}(\lambda)$, which can then be compared to the response-corrected experimental spectrum to obtain the plasma parameters

Theoretical and empirical model

Theoretical plasma models exist, e. g., for argon [15–28] and xenon [25, 29–38]. A possible use of such a model for extracting plasma parameters from optical emission spectra is shown schematically in Fig. 1. Such models are typically tailored for a specific application. For other applications, such as using other gases, the theoretical model needs to be modified.

In electric propulsion, alternative propellants such as krypton and iodine gain considerable interest [39, 40]. In case of molecular propellants like iodine I_2 these models would become increasingly complex. For a successful description of the corresponding plasma, such a microscopic model requires many microscopic input parameters like excitation cross sections for all relevant species, including I_2, I_2^+, I^+, I^- in case of an iodine plasma.

Furthermore, the microscopic parameters serving as basis of such a model like, for instance, transition matrix elements, scattering cross sections etc. are usually not accurately known, as they are, in many cases, difficult to derive theoretically and to verify experimentally. Typically, some simplifications and assumptions are made to compensate the lack of information and to reduce the complexity of the model. Heavy gases like xenon have a large number of electronic states. Ref. [41] lists 443 levels for neutral Xe, 161 for Xe^+, 157 for Xe^{2+} and a lot more for higher ionized xenon ions. Since not all of these levels are relevant in a real plasma, only some levels are considered in the modeling (e. g., 173 levels in Ref. [33] or 38 levels in Ref. [38]). So the number of considered levels can vary from one model to another. Neglecting levels may, however, cause errors in the calculated

population of other related levels. Another typical simplification is the negligence of uncommon excitation processes like ion-atom collisions or excitation from meta-stable states. However, these processes are necessary in some cases to yield a reliable correlation between OES and plasma parameters [30]. Whether a simplification or assumption in a model is justified can only be verified by a direct comparison with experiments.

Therefore, we decided to avoid the microscopic modeling entirely and correlate the optical spectrum directly to measured plasma parameters using multivariate data analysis techniques. In contrast to the theoretical plasma model, our empirical approach does not require any microscopic input other then the measurement of the plasma parameters. A schematic description of our approach is shown in Fig. 2. We measure a reference data set of emission spectra simultaneously with the plasma parameters in a RIT like setup operating with a propellant plasma, such as xenon. A Langmuir diagnostics is permanently installed inside the discharge vessel. Using a Langmuir double probe [42] the electron temperature and density can be measured. The analysis of the OES reference data is performed by applying a PCA [8]. The results from both measurements are analyzed and a one-to-one correlation between the principal components and the electron temperature and the electron/ion density is established. This correlation can be employed to extract plasma parameters non-invasively from plasmas operating under similar conditions as the reference plasma, for instance, inside a thruster. For this purpose, an optical emission spectrum $S'(\lambda)$ is measured and expanded in terms of the PC of the reference data to yield its PC scores. Then, using the established correlation between PC scores and plasma parameters, n'_e and T'_e, corresponding to $S'(\lambda)$ can be obtained.

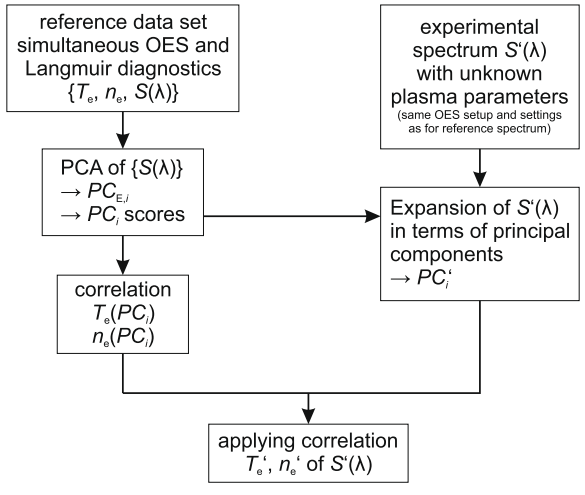

Fig. 2 Schematic description of our measurement-based correlation between optical emission spectrum and plasma parameters. First, a reference data set is measured consisting of simultaneously performed OES and Langmuir diagnostics. The measured spectrum is transferred into a simplified coordinate system using PCA, which yields the axes $PC_{E,i}$ and the coordinates or scores PC_i of the spectra on these axes. The scores PC_i are then correlated with the measured plasma parameters. The correlation can then be used to extract plasma parameters from a measured spectrum $S'(\lambda)$ by calculating its scores PC'_i and inserting them into the correlation

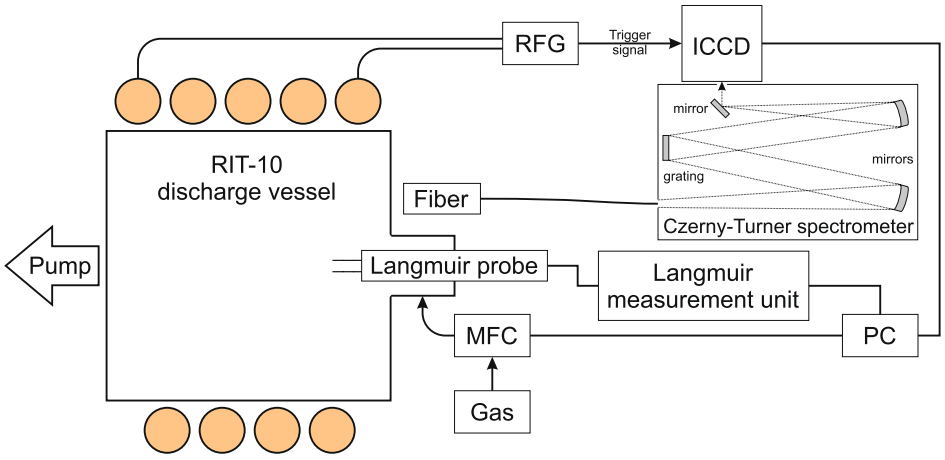

Fig. 3 Experimental setup for simultaneous optical emission spectroscopy and the Langmuir double probe measurements

Experimental details and theory

The experimental setup used is shown in Fig. 3. An inductively generated plasma is ignited in a 10 cm diameter cylindrical quartz glass discharge vessel of a RIT-10. Basically, it is a RIT-10 without an extraction system or surrounding vacuum. The gas inlet in this setup also contains the Langmuir double probe, which is used to determine the electron temperature T_e and density n_e [6, 7, 42] . The glass vessel facilitates an easy optical access to the plasma from behind. The spectrum was measured at a position close to the Langmuir probe. The Czerny-Turner spectrometer used is connected to an intensified charge-coupled device (ICCD) camera. In the observed spectral window from 820 to 840 nm the system has a resolution of approximately 28 pm/pixel. This spectral window was chosen, since neutral xenon has several strong lines in the near-infrared region. Six of them lie in the observed window. The ICCD is capable of both continuous-wave (cw) and time-resolved measurements on the nanosecond scale and was operated with 20 ns time resolution here, i.e., the acquisition time was 20 ns long after a predefined time delay. The corresponding trigger was a 0 to 5 V rectangular signal taken from the radio-frequency generator (RFG). For each delay time, several 100 acquisitions were recorded and accumulated. By varying the delay time in the range of 600 to 1400 ns a series of optical emission spectra is obtained which covers the time evolution of the plasma parameters during one RF excitation cycle. The gas flow into the discharge vessel is controlled by a mass flow controller (MFC). The plasma was excited by the RFG at a resonance frequency of approximately 1.2 MHz corresponding to a period of the RF cycle of 0.83 μs. The RFG input power was varied while keeping the gas flow constant. The experiments were performed for various gas flows.

An example of a cw OES measurement is shown as an inset in Fig. 4. The six xenon lines, (1) to (6) are assigned to the optical transitions between Xe^0 states using the NIST data base [43]. The electronic states involved are shown in the main graph. The upper levels of the six transitions observed in this experiment can be populated either by direct excitation or by another spectral transition (the strongest are shown in Fig. 4). In Table 1, wavelength position, relaxation time, qualitative relative intensity and the involved electronic states are given for each transition according to the data provided in Ref. [41] and [43].

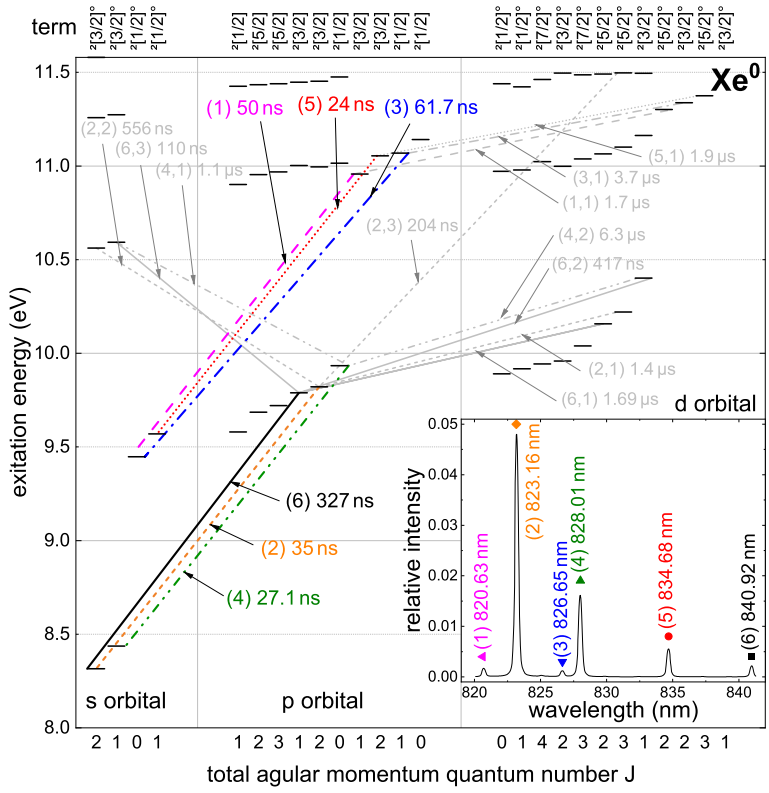

Fig. 4 The measured spectral range from 820 nm to 841 nm exhibits six xenon transitions, which are shown in the energy level scheme for neutral xenon generated from the data from Ref. [41]. A corresponding example spectrum is shown in the inset. The strongest transitions feeding the upper levels of the observed transitions are also shown. The relaxation times of the transitions are given according to Ref. [43]. Using the labeling given in the figure, the transitions can be found in Table 1 for additional details

As examples a series of cw OES measurements is shown in Fig. 5a with the corresponding Langmuir double probe measurements in Fig. 5b. Here, the RF input power was varied at a constant gas flow of 0.1 sccm.

The line intensity ratios differ only slightly in the spectra shown in Fig. 5a. All spectra were intensity-normalized over the measured range. The effect can be observed best for the two strongest lines at 823.2 nm and 828.0 nm. Here, the 823.2 nm line increases with higher input power, while the 828.0 nm line decreases. The plasma parameters determine the population of the energy levels. At different operating points with different plasma parameters the levels are populated differently with electrons, resulting in other line ratios when the electrons recombine radiatively.

Principal component analysis

Instead of founding the analysis on individual line ratios, we made use of the entire spectral information in terms of relative intensities available in a spectrum of a given operational point by performing a PCA of all spectra [8]. The PCA technique can simplify the complex correlations between several measured lines and the resulting plasma parameters by reducing the dimensions of the data set. Similar techniques for dimension reduction which may offer an alternative and may also yield satisfying results are Linear

Table 1 Wavelengths, relaxation times, intensities and the involved electronic states of the transitions shown in Fig. 4 are listed [41, 43]

index	wavelength (nm)	relaxation time (ns)	intensity	lower level			upper level		
				configuration	term	J	configuration	term	J
(1)	**820.63**	**50**	**700**	$\mathbf{5p^5(^2P^o_{1/2})6s}$	$\mathbf{^2[1/2]^\circ}$	**0**	$\mathbf{5p^5(^2P^o_{1/2})6p}$	$\mathbf{^2[3/2]}$	**1**
(1,1)	3605.49	1700	20	$5p^5(^2P^o_{1/2})6p$	$^2[3/2]$	1	$5p^5(^2P^o_{1/2})5d$	$^2[5/2]^\circ$	2
(2)	**823.16**	**35**	**10000**	$\mathbf{5p^5(^2P^o_{3/2})6s}$	$\mathbf{^2[3/2]^\circ}$	**2**	$\mathbf{5p^5(^2P^o_{3/2})6p}$	$\mathbf{^2[3/2]}$	**2**
(2,1)	3107.77	1400	6000	$5p^5(^2P^o_{3/2})6p$	$^2[3/2]$	2	$5p^5(^2P^o_{3/2})5d$	$^2[5/2]^\circ$	3
(2,2)	1672.82	556	5000	$5p^5(^2P^o_{3/2})6p$	$^2[3/2]$	2	$5p^5(^2P^o_{3/2})7s$	$^2[3/2]^\circ$	2
(2,3)	739.38	204	150	$5p^5(^2P^o_{3/2})6p$	$^2[3/2]$	2	$5p^5(^2P^o_{3/2})7d$	$^2[5/2]^\circ$	3
(3)	**826.65**	**61.7**	**500**	$\mathbf{5p^5(^2P^o_{1/2})6s}$	$\mathbf{^2[1/2]^\circ}$	**1**	$\mathbf{5p^5(^2P^o_{1/2})6p}$	$\mathbf{^2[1/2]}$	**1**
(3,1)	4610.87	3700	1	$5p^5(^2P^o_{1/2})6p$	$^2[1/2]$	1	$5p^5(^2P^o_{1/2})5d$	$^2[3/2]^\circ$	2
(4)	**828.01**	**27.1**	**7000**	$\mathbf{5p^5(^2P^o_{3/2})6s}$	$\mathbf{^2[3/2]^\circ}$	**1**	$\mathbf{5p^5(^2P^o_{3/2})6p}$	$\mathbf{^2[1/2]}$	**0**
(4,1)	1878.82	1100	860	$5p^5(^2P^o_{3/2})6p$	$^2[1/2]$	0	$5p^5(^2P^o_{3/2})7s$	$^2[3/2]^\circ$	1
(4,2)	2651.77	6300	30	$5p^5(^2P^o_{3/2})6p$	$^2[1/2]$	0	$5p^5(^2P^o_{3/2})5d$	$^2[3/2]^\circ$	1
(5)	**834.68**	**24**	**2000**	$\mathbf{5p^5(^2P^o_{1/2})6s}$	$\mathbf{^2[1/2]^\circ}$	**1**	$\mathbf{5p^5(^2P^o_{1/2})6p}$	$\mathbf{^2[3/2]}$	**2**
(5,1)	3869.68	1900	200	$5p^5(^2P^o_{1/2})6p$	$^2[3/2]$	2	$5p^5(^2P^o_{1/2})5d$	$^2[5/2]^\circ$	3
(6)	**840.92**	**327**	**2000**	$\mathbf{5p^5(^2P^o_{3/2})6s}$	$\mathbf{^2[3/2]^\circ}$	**2**	$\mathbf{5p^5(^2P^o_{3/2})6p}$	$\mathbf{^2[3/2]}$	**1**
(6,1)	3367.59	1690	3500	$5p^5(^2P^o_{3/2})6p$	$^2[3/2]$	1	$5p^5(^2P^o_{3/2})5d$	$^2[5/2]^\circ$	2
(6,2)	2026.78	417	2300	$5p^5(^2P^o_{3/2})6p$	$^2[3/2]$	1	$5p^5(^2P^o_{3/2})5d$	$^2[3/2]^\circ$	1
(6,3)	1541.8	180	110	$5p^5(^2P^o_{3/2})6p$	$^2[3/2]$	1	$5p^5(^2P^o_{3/2})7s$	$^2[3/2]^\circ$	1

The listed intensities are only the qualitative vf. [41]. Using the index, the transitions can be found in Fig. 4. The observed transitions are shown in bold

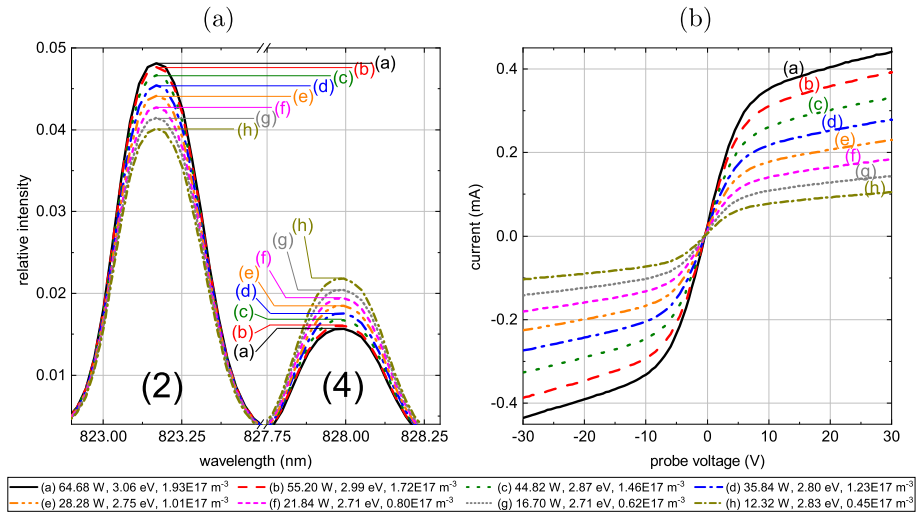

Fig. 5 The two strongest lines (see Fig. 4) of intensity-normalized xenon spectra for a measurement series at 0.1 sccm gas flow at different operating points (see also Fig. 6) (**a**) together with the corresponding Langmuir double probe measurements (**b**). This series of spectra is part of the reference data set

Discriminant Analysis [44], Non-negative Matrix Factorization [45] and Factor Analysis [46].

A total of m spectra is measured as a reference data set. A spectrum consists of n data points, i. e., n wavelength positions and corresponding emission intensity values. Each of the m spectra yields a data point in an n-dimensional space, where each of the n wavelength positions of the spectrum corresponds to one coordinate axis and the intensity value to the specific coordinate on that axis. The PCA simplifies the data by reducing this n-dimensional space into, for example, a two-dimensional space, that represents the data best. This is done by finding the axes with the highest variance in the data.

First, the average spectrum of the entire reference data set $\overline{S_{\mathrm{PCA}}}(\lambda)$ is subtracted from each spectrum $S(\lambda)$. To derive the new coordinates, i. e., the PCA-axes, the covariances σ_{ij} of each of the n wavelength positions with every other wavelength position (including itself) are calculated using

$$\sigma_{ij} = \frac{1}{m} \cdot \sum_{k=0}^{m} (x_{ki} - \overline{x_i}) \cdot (x_{kj} - \overline{x_j}) \quad \text{where } \overline{x_i} = \overline{x_j} = 0. \tag{1}$$

Here, x_{ki} and x_{kj} are the values of wavelength positions i and j of the spectrum k. Since the average intensities of each wavelength position $\overline{x_i}$ and $\overline{x_j}$ were already subtracted before, they are now zero.

With these covariances the covariance matrix $\mathbf{C}$ is set up

$$\mathbf{C} = \begin{pmatrix} \sigma_{00} & \sigma_{01} & \cdots & \sigma_{0n} \\ \sigma_{10} & \sigma_{11} & \cdots & \sigma_{1n} \\ \vdots & \vdots & \ddots & \vdots \\ \sigma_{n0} & \sigma_{n1} & \cdots & \sigma_{nn} \end{pmatrix}. \tag{2}$$

Diagonalizing $\mathbf{C}$ yields its eigenvalues, which correspond to the variance of the data on the principal component axes $PC_{\mathrm{E},i}(\lambda)$. The PC-axes are the eigenvectors of $\mathbf{C}$.

To transfer a spectrum into the new coordinate system spanned by the eigenvectors $PC_{\mathrm{E},i}(\lambda)$ and obtain its coordinates, i. e., the PC scores, the spectrum is scalar multiplied with each eigenvector

$$PC_i = \sum_{\lambda} (S(\lambda) - \overline{S_{\mathrm{PCA}}}(\lambda)) \cdot PC_{\mathrm{E},i}(\lambda). \tag{3}$$

The spectrum can now be written as

$$S(\lambda) = \overline{S_{\mathrm{PCA}}}(\lambda) + \sum_{i} PC_i \cdot PC_{\mathrm{E},i}(\lambda). \tag{4}$$

The percentage of the variance on each axis of the total variance shows how well the data is represented. If the sum of the variances of PC_1 and PC_2 is already close to the total variance, these two axes are sufficient to describe the main differences in the data.

Evaluation of the Langmuir probe measurements

The plasma parameters obtained from the Langmuir double probe measurements were evaluated using a modified version of the standard procedure described in Ref. [6], [7] and [42], which is more robust against deviations from the theoretical ideal. First, the ion saturation current I_{sat} is determined as the intercept of a linear fit of the saturation region (approximately $< -20\,\mathrm{V}$ and $> +20\,\mathrm{V}$ in Fig. 5b). The slope a of the fit is subtracted from the measured U-I-characteristic ($I_{\mathrm{corrected}}(U) = I(U) - a \cdot U$). Afterwards, $I_{\mathrm{corrected}}(U)$ is divided by I_{sat} to normalize the U-I-characteristic. Next, the electron temperature T_{e} is extracted from the maximum slope. A polynomial fit of third order ($f(x) = \sum_{i=0}^{3} a_i \cdot x^i$) around $U = 0 \pm \Delta U$ is used instead of a linear fit, because the resulting slope is less affected by the chosen fit bounds ΔU. The maximum slope of this fit is given with $s_{\mathrm{max}} = -\frac{1}{3}a_2^2/a_3 + a_1$ and yields the electron temperature according to

$$T_{\mathrm{e}} = \frac{e}{2k_{\mathrm{B}} \cdot s_{\mathrm{max}}}. \tag{5}$$

The electron density n_{e} is calculated from I_{sat}, T_{e}, the probe area A_{p}, and the ion mass m_{ion} according to

$$n_{\mathrm{e}} = \frac{I_{\mathrm{sat}}}{A_{\mathrm{p}} e} \sqrt{\frac{m_{\mathrm{ion}}}{k_{\mathrm{B}} T_{\mathrm{e}}}}. \tag{6}$$

It should be noted that the definition of a temperature assumes a Maxwellian electron energy distribution function (EEDF) [6, 7, 42]. For an RF plasma, the EEDF can deviate from the Maxwellian ideal, as the fast electrons in the Maxwell tail are suppressed [21, 47]. In particular in a theoretical microscopic plasma model, the EEDF can have a major impact on the calculated spectrum and therefore on the extraction of plasma parameters by comparison between microscopic model and experiment. In case of our empirical approach the specific EEDF is not relevant, as long as it is comparable in model setup and later measurement, which should be the case when the optical emission spectra are comparable.

Results and discussion

Before performing the PCA, the measured spectra are compressed by considering only the intensities or areas of the spectral lines (see e. g. Figs. 4 or 5a). This prevents small wavelength shifts in the range of several tens of picometers to influence the PCA result. The line intensities are then used as input variables for the PCA. The PCA yields a set

of new orthogonal coordinate axes, i. e., the principal components $PC_{E,i}$ ($i = 1,...,n$), along which the spread in the data set is maximum, as they are the eigenvectors of the variance. The $PC_{E,i}$ are numbered serially to descending variance weight, i. e., $PC_{E,1}$ carries the highest weight, followed by $PC_{E,2}$ etc. Often, the first few $PC_{E,i}$ already collate most of the variance (e. g., 90 %), and thus plots of the PC scores of a spectrum in a low-dimensional coordinate system spanned by those $PC_{E,i}$ can separate the data adequately. In case of our data, $PC_{E,1}$ and $PC_{E,2}$ are sufficient to fully distinguish between the spectra obtained at different operational points of the plasma, i. e., corresponding to different plasma parameters. The results are shown in Fig. 6a. It can be seen that the individual data points are clearly separated. The cloud of data points representing all spectra analyzed has a "triangular" shape. Towards lower PC_1-values, the plasma extinguished. Towards higher PC_1-values the input power limitation of the RFG was reached. The plasma is stable even at lower input powers at higher gas flows. Therefore, more measurements were possible at higher PC_2-values. With decreasing gas flow towards lower PC_2-values, the

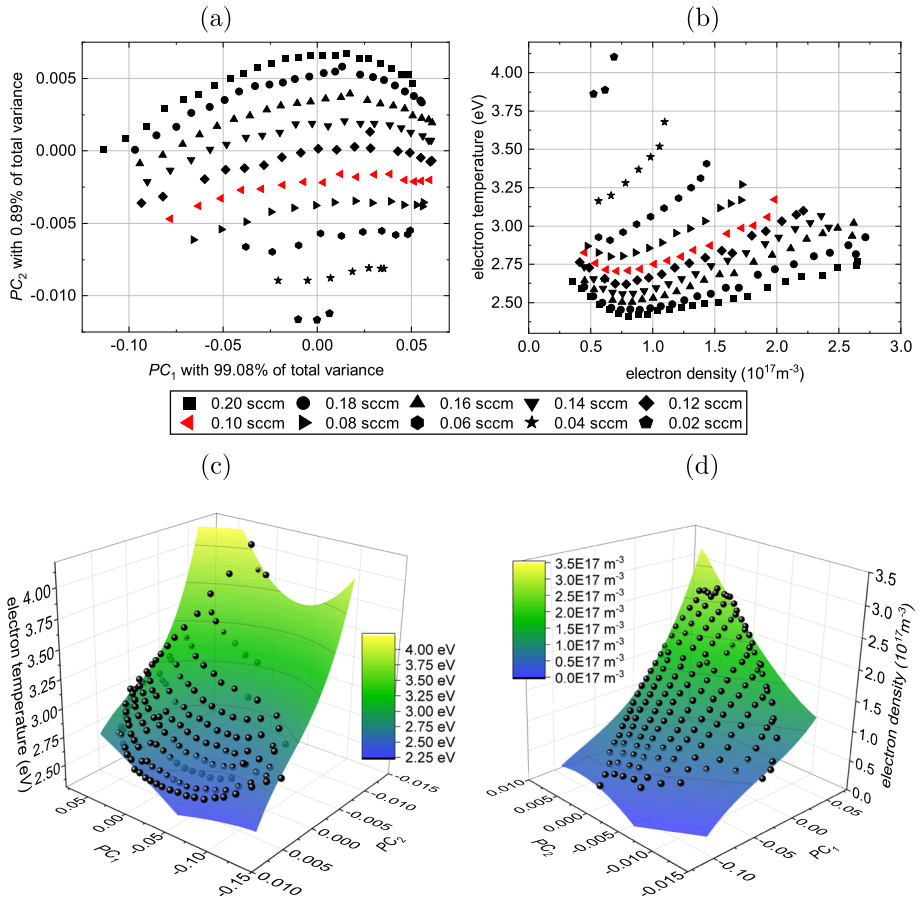

Fig. 6 PCA scores from the cw OES measurements of a xenon plasma (**a**) and the corresponding electron temperatures and densities from the simultaneously conducted Langmuir double probe measurements (**b**). The PCA scores of the spectra shown in Fig. 5a from the 0.10 sccm measurement series (shown in red here) are clearly distinguishable. The input power increases from left to right in both plots (a) and (**b**). The fits of the electron temperature (**c**) and density (**d**) over the PCA scores are the depict correlation between OES and plasma parameters

minimum power to sustain the plasma increased, until eventually reaching the RFG input power limit. Therefore, only a few points could be measured in this range.

The plasma parameters electron temperature T_e and electron density n_e corresponding to each spectrum from the Langmuir measurements are shown in Fig. 6b. Here, the cloud of data points also exhibits a triangular arrangement. The reason for this shape is the same as discussed above for the PCA data in Fig. 6a.

While the data points are spread quite homogeneously in Fig. 6a, the data sets corresponding to various gas flows in Fig. 6b are very close for low T_e and far apart for high T_e. This means that the sensitivity of T_e on the neutral gas density increases with decreasing gas flow. This change in sensitivity on the gas flow can barely be observed for the OES data in Fig. 6a. In a series of spectra where the RFG input power was varied, the corresponding data points are rather equally distributed, resulting from constant steps of the RFG input voltage. The data points plotted by red symbols in Fig. 6a and b correspond to the series of optical emission spectra and corresponding Langmuir measurements shown in Fig. 5a and b, respectively. It can be seen that the red data points string together well underlining that the PCA and the restriction to the PC scores of $PC_{E,1}$ and $PC_{E,2}$ grabs the differences in the spectra sufficiently to clearly distinguish between them.

By using a polynomial fit of the form given in Eq. (7) the plasma parameters from Fig. 6b can be described as a function of the PCA-scores from Fig. 6a, yielding the sought correlation

$$f(PC_1, PC_2) = \sum_{i=0}^{3} \sum_{j=0}^{i+j\leq 3} a_{i,j} \cdot PC_1^i \cdot PC_2^j. \tag{7}$$

The fitted surfaces for the electron temperature and density versus the scores of PC_1 and PC_2 are shown in Fig. 6c and d, respectively. The R^2-values of the fitting procedures were 0.984 (T_e) and 0.998 (n_e), so the fitted surfaces are well suited for describing the measured data. The choice of a polynomial fitting surface of order 3 is the result of an optimization process. In other cases, such as other propellant gases or the choice of another spectral window, fitting with lower or higher polynomials may turn out the best choice.

To apply this correlation to a measured spectrum $S'(\lambda)$ for which the plasma parameters are not known, the eigenvectors of the PCA $PC_{E,i}(\lambda)$ are needed in order to extract them. The eigenvectors are scalar multiplied with the spectrum $S'(\lambda)$ from which the average of the intensities initially used for the PCA $\overline{S_{PCA}}(\lambda)$ are subtracted, as shown in Eq. (3). The resulting coordinates of PC_1 and PC_2 can then be inserted into the polynomial expressions describing the fitted surfaces $T_e(PC_1, PC_2)$ and $n_e(PC_1, PC_2)$ shown in Fig. 6c and d to obtain T_e' and n_e' corresponding to $S'(\lambda)$.

In order to minimize experimental uncertainties the optical spectra and Langmuir parameters were measured at almost the same position inside the plasma (see Fig. 3). It is essential to keep the deviations between the spots probed by OES and the Langmuir probe as small as possible, because the plasma parameters may vary locally inside the vessel. A large distance between the measurement positions introduces uncertainties when employing the established correlation for extracting plasma parameters from another system. In principle, the correlation may be employed on any other Xe plasma source where the plasma parameters lie in the same range as used here for establishing the correlation. Having established a reliable correlation, it can be used to spatially monitor the plasma

parameter variation inside a plasma vessel. For example, such spatial mapping will further benefit the understanding of the processes inside an ion thruster.

The relaxation times of the observed transitions are in the range of 24 to 327 ns and even longer in case of radiative transitions whose higher electronic state is fed by other higher lying states (see Fig. 4 or Table 1). Compared to the RF period of approximately 833 ns, not all of these times are significantly shorter. This can cause different relative line intensities, when the plasma is driven with another radio frequency, and the population of the electronic states cannot follow the RF excitation. Because of such effects, it is of paramount importance to make sure that reference spectra and probe spectra are recorded with the corresponding plasmas driven by the same radio frequency.

Time-resolved measurements

The time dependence of the example OES measurement from Fig. 4 is shown in Fig. 7. The graph shows the variation of the line intensities obtained from a series of optical emission spectra taken at different delay times. Here, the integrated line intensities of the six strongest lines in the spectrum are plotted as the relative deviation from their corresponding average value during one RF cycle. The intensity of each line oscillates about its average value with twice the radio frequency. This is anticipated as the power input is proportional to the RF field squared. During one RF cycle, the electrons are accelerated the most at the maximum and minimum electric field, but in opposite directions. The excitation of the gas atoms and ions in the discharge chamber is strongest at these two points in

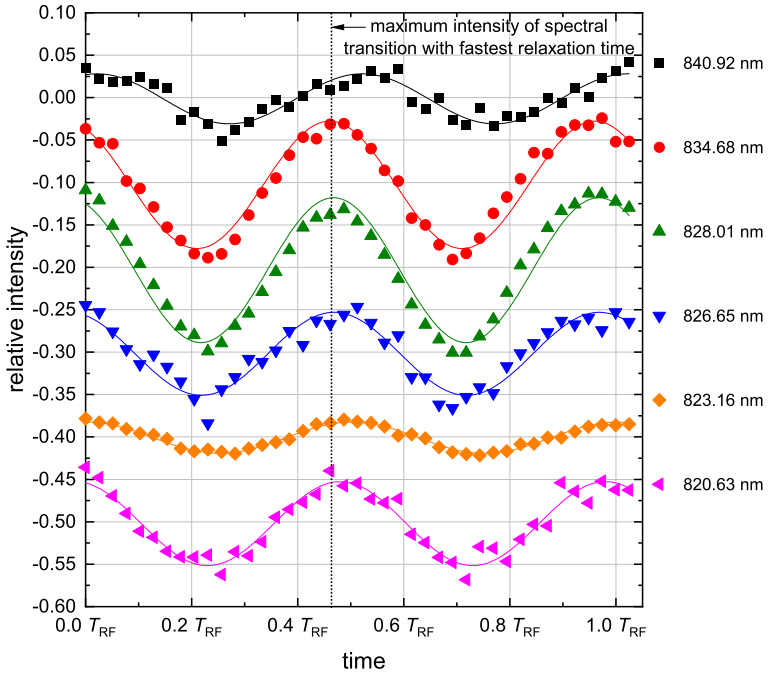

Fig. 7 Time evolution of the intensities obtained from a series of spectra taken at different time delays. The average spectrum of this series is shown in Fig. 4. The intensities are divided by the corresponding average line intensity and shifted by 0.1 towards each other for better visibility. The local maximum of the spectral transition with the fastest relaxation time is indicated by the dashed line. The slower spectral transitions show a small phase shift of approximately 10 to 30 ns (except 840.92 nm, where it is slightly more). The radio frequency driving the plasma was 1.281 MHz, so $T_{RF} = 780$ ns

time and weakest at times when the electric field crosses zero, resulting in an oscillation with twice the radio frequency as visible in Fig. 7.

Assuming that the time response of the electron system to changes of the RF excitation is faster than 20 ns, we can assume that each emission spectrum taken at a specific time delay is characterized by a set of plasma parameters. Thus, time-resolved OES measurements like those shown in Fig. 7 can be evaluated using the correlation method described above to obtain the time-evolution of the plasma parameters during one RF cycle. However, it should be noted that some of the excitation and relaxation processes leading to the optical spectra possess characteristic times on the nanosecond scale leading to a phase shift between the cosine curves describing the intensity variation in Fig. 7. If a relaxation time is very long compared to the oscillation period, the phase of the oscillation will lack behind and its amplitude will flatten, eventually down to zero [11–13]. When comparing the oscillations of the 840.92 nm and the 828.01 nm lines in Fig. 7, which have 327 ns and 27.1 ns [43] relaxation times, respectively (see Fig. 4 or Table 1), this effect already starts to occur. A similar phase shift can be observed for the 823.16 nm line which has a relaxation time of 35.0 ns [43]. This is still short compared to the approximately 390 ns oscillation period and indicates, that the upper level of the 823.16 nm line is not excited directly, but is fed through one or several higher lying electronic states with longer relaxation times, as shown in Fig. 4 or Table 1. The free electrons are able to follow the RF, so the excitation of the electronic states should follow, too. The relaxation of the electronic states on the other hand cannot necessarily follow. For now, we will assume that the evaluation of the time-resolved optical spectra is a valid approach, since the phase shift of the intensity oscillations in Fig. 7 against each other of approximately 10 to 30 ns are rather short compared to the oscillation period of, in this case, 390 ns. Whether this leads to a reliable determination of time-resolved plasma parameters has yet to be verified, for instance, by a PIC (particle in cell) modeling of the microscopic processes inside the plasma. A set of lines with faster relaxation times or lower RF frequencies will reduce the errors made.

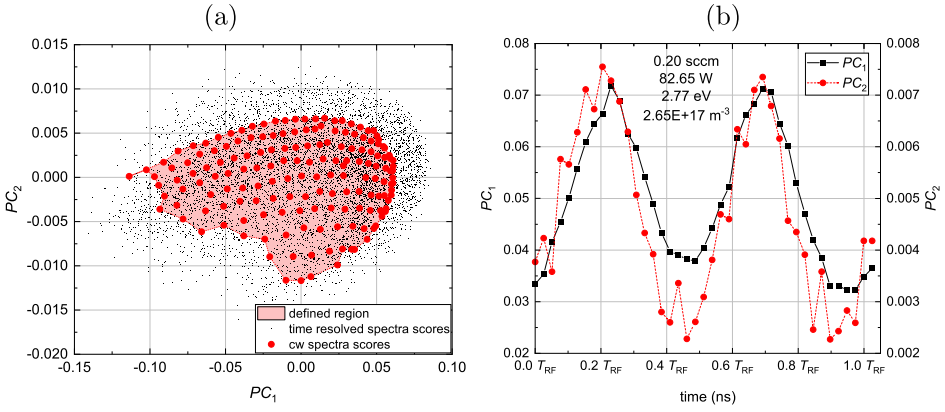

Fig. 8 PCA scores of the time-resolved optical emission measurements for a xenon plasma driven with 1.2 MHz RF excitation (**a**). The defined region that is mapped by the scores of the cw optical emission spectra from which the correlation has been established is shown in red. Scores of time-resolved spectra outside this region cannot reliably be used to estimate plasma parameters as they lie outside the area where the one-to-one correlation was established and fitted. Plasma parameters extracted from the fitting in this range are uncertain. The oscillation of the PCA scores as a function of delay time is shown in (**b**) for a series of time-resolved spectra. Mass flow, RF input power and average electron temperature and density are given in the plot. PC_1 and PC_2 oscillate with twice the radio frequency as the corresponding line intensities in Fig. 7

To extract the time evolution of the plasma parameters from the optical emission spectra taken at different time delays, the PCA scores for the series of spectra need to be calculated with respect to the PCA eigenvectors derived from the cw measurements. The PCA scores are obtained by scalar multiplication with the PCA eigenvectors of the cw measurements as described in equation (3) and are shown in Fig. 8a. It can already be seen that some PCA scores in Fig. 8a lie outside of the mapped area of the cw data for which the correlation with the plasma parameters was established by the fits. Therefore, the plasma parameters extracted for these data points employing the fitted correlation will be rather unreliable. Nevertheless, plotting the scores of the PC_1 and PC_2 values obtained as a function of delay time yields an oscillating behavior with twice the radio frequency (see Fig. 7b).

With the PCA scores calculated the polynomial fitting functions describing the parameter surfaces in Fig. 6c and d are used to translate these scores into plasma parameters as described by Eq. (7). This way, the time evolution of the plasma parameters during one RF cycle can be obtained. Some examples of such time evolutions are shown in Fig. 9. Note that some measurements yield rather stable results, while others are mostly estimations since their PCA-scores are outside the reliable region defined by the cw measurements shown in Fig. 8a. In Fig. 9a it can be seen that the amplitude of the electron density oscillation during an RF cycle increases with increasing average electron density, i.e., with increasing RF input power. The electron temperature in Fig. 9b, on the other hand, is almost constant over the RF cycle for the curves obtained from series of spectra at higher RF input power. In contrast, the two curves obtained from series of spectra at lower input power exhibit strong oscillations. Such strong oscillations in electron temperature may lead to a sputtering rate of the RIT screen grid that is higher than anticipated from the average electron temperature.

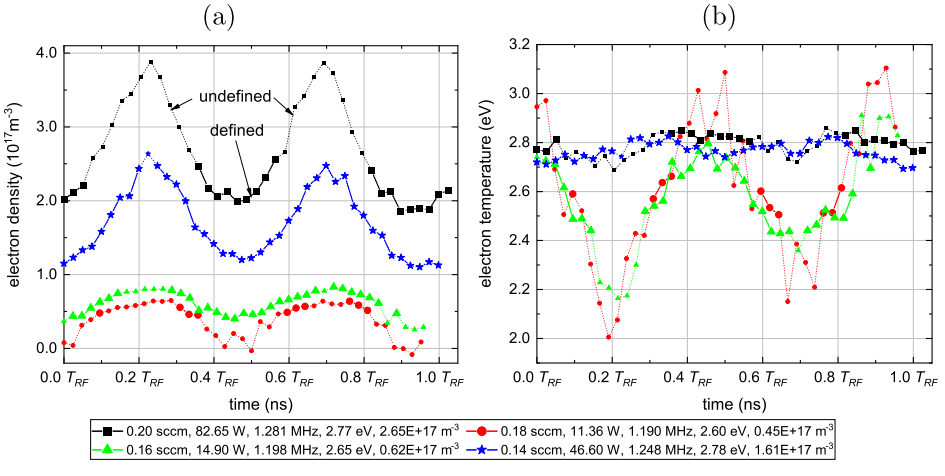

Fig. 9 Plots of the time evolution of electron density (**a**) and temperature (**b**) for a xenon plasma driven by 1.2 MHz RF excitation for various operation parameters calculated from the PCA scores (see Fig. 8b) of time-resolved optical spectra (see Fig. 7). Mass flow, RF input power, frequency as well as average electron temperature and density are given in the legend. Parameters resulting from data points outside the mapped region (see Fig. 8a) are ill defined and plotted as smaller symbols connected by a dotted line. The plasma parameters oscillate with twice the radio frequency

Conclusion

A method of non-invasively extracting plasma parameters from an OES using a correlation based on a reference data set of simultaneously recorded optical emission spectra and Langmuir measurements has been presented and validated. The method utilizes the high sensitivity of a PCA to detect small and multi-dimensional changes occurring in the emission spectra of the plasma inside an ion thruster at different operational points. The PCA results are fitted to plasma parameters obtained by Langmuir measurements yielding a one-to-one correlation. Using this correlation, plasma parameters can be determined with just the non-invasive OES measurement. We have also demonstrated that our correlation approach can be used to monitor the time-evolution of the plasma parameters in an RF plasma, electron temperature and density, during an RF cycle. Knowledge of the time dependence of plasma parameters will help to identify critical operation points of RITs and other thrusters and to optimize their performance. Furthermore, it will yield valuable input parameters for theory, i.e., help to further develop theoretical models of such thrusters. In addition, the approach is not restricted to xenon as propellant and may be also employed in case of alternative propellants such as krypton or iodine. Typically, the plasma parameters also vary spatially inside a macroscopic plasma vessel. Thus, the approach described has the potential to spatially resolve the distribution of plasma parameters inside a plasma vessel. Carefully conducted, our approach provides a powerful tool for determining the plasma parameters non-invasively by OES without having to rely on microscopic modeling.

Abbreviations

RIT: Radio-frequency Ion Thruster; OES: Optical Emission Spectroscopy; PCA: Principal Component Analysis; PC: Principal Component; EP: Electric Propulsion; ICCD: Intensified Charge-Coupled Device; cw: continuous wave; RFG: Radio-Frequency Generator; RF: Radio-Frequency; MFC: mass flow controller; NIST: National Institute of Science and Technology; EEDF: Electron Energy Distribution Function

Acknowledgements

Benny Nauschütt is grateful for receiving a PhD studentship in the framework of the JLU-Ariane Group Graduate School "Radiofrequency ion thrusters".

Authors' contributions

BN wrote the manuscript and performed and evaluated the measurements. LC assisted in evaluating the OES measurements using PCA. KH and PJK supervised the activities and provided the idea for the experiment. All authors contributed to data interpretation and discussion. All authors read and approved the final manuscript.

Funding

Open Access funding enabled and organized by Projekt DEAL.

Availability of data and materials

The data sets used and/or analyzed during the current study are available from JLUdata under the link "http://dx.doi.org/10.22029/jlupub-54".

Declarations

Ethics approval and consent to participate

Not applicable.

Consent for publication

All authors agree to the publication of the article.

Competing interests

The authors declare that they have no competing interests.

Received: 31 May 2021 Accepted: 17 July 2021
Published online: 05 August 2021

References

1. Mazouffre S. Electric propulsion for satellites and spacecraft: established technologies and novel approaches. Plasma Sources Sci Technol. 2016;25(3):033002. https://doi.org/10.1088/0963-0252/25/3/033002.
2. Holste K, Dietz P, Scharmann S, Keil K, Henning T, Zschätzsch D, Reitemeyer M, Nauschütt B, Kiefer F, Kunze F, Zorn J, Heiliger C, Joshi N, Probst U, Thüringer R, Volkmar C, Packan D, Peterschmitt S, Brinkmann K-T, Zaunick H-G, Thoma MH, Kretschmer M, Leiter HJ, Schippers S, Hannemann K, Klar PJ. Ion thrusters for electric propulsion: Scientific issues developing a niche technology into a game changer. Rev Sci Instrum. 2020;91(6):061101. https://doi.org/10.1063/5.0010134.
3. Löb H. Ein elektrostatisches Raketentriebwerk mit Hochfrequenzionenquelle. Astronautica Acta. 1962;8(1):49.
4. Löb H, Freisinger J. Ionenraketen. Braunschweig: Vieweg+Teubner Verlag; 1967.
5. Goebel DM, Katz I. Fundamentals of Electric Propulsion. 1st ed. Hoboken: Wiley; 2008.
6. Demidov VI, Ratynskaia SV, Rypdal K. Electric probes for plasmas: The link between theory and instrument. Rev Sci Instrum. 2002;73(10):3409–39. https://doi.org/10.1063/1.1505099.
7. Benedikt J, Kersten H, Piel A. Foundations of measurement of electrons, ions and species fluxes toward surfaces in low-temperature plasmas. Plasma Sources Sci Technol. 2021;30(3):033001. https://doi.org/10.1088/1361-6595/abe4bf.
8. Abdi H, Williams LJ. Principal component analysis. Wiley Interdiscip Rev Comput Stat. 2010;2(4):433–59. https://doi.org/10.1002/wics.101.
9. Tartz M, Hartmann E, Neumann H. Evolution of Extraction Grid Erosion with Operation Time. In: 40th AIAA/ASME/SAE/ASEE Joint Propulsion Conference and Exhibit. American Institute of Aeronautics and Astronautics; 2004. https://doi.org/10.2514/6.2004-3787.
10. Sangregorio M, Xie K, Wang N, Guo N, Zhang Z. Ion engine grids: Function, main parameters, issues, configurations, geometries, materials and fabrication methods. Chin J Aeronaut. 2018;31(8):1635–49. https://doi.org/10.1016/j.cja.2018.06.005.
11. de Rosny G, Mosburg ER, Abelson JR, Devaud G, Kerns RC. Evidence for a time dependent excitation process in silane radio frequency glow discharges. J Appl Phys. 1983;54(5):2272–5. https://doi.org/10.1063/1.332381.
12. Gottscho RA, Miller TA. Optical techniques in plasma diagnostics. Pure Appl Chem. 1984;56(2):189–208. https://doi.org/10.1351/pac198456020189.
13. Flamm DL, Donnelly VM. Time-dependent excitation in high- and low-frequency chlorine plasmas. J Appl Phys. 1986;59(4):1052–62. https://doi.org/10.1063/1.336541.
14. Schulze J, Schüngel E, Donkó Z, Luggenhölscher D, Czarnetzki U. Phase resolved optical emission spectroscopy: a non-intrusive diagnostic to study electron dynamics in capacitive radio frequency discharges. J Phys D Appl Phys. 2010;43(12):124016. https://doi.org/10.1088/0022-3727/43/12/124016.
15. Vlcek J. A collisional-radiative model applicable to argon discharges over a wide range of conditions. I, Formulation and basic data. J Phys D Appl Phys. 1989;22(5):623–31. https://doi.org/10.1088/0022-3727/22/5/009.
16. Vlcek J, Pelikan V. A collisional-radiative model applicable to argon discharges over a wide range of conditions. II, application to low-pressure, hollow-cathode arc and low-pressure glow discharges. J Phys D Appl Phys. 1989;22(5):632–43. https://doi.org/10.1088/0022-3727/22/5/010.
17. Bogaerts A, Gijbels R, Vlcek J. Collisional-radiative model for an argon glow discharge. J Appl Phys. 1998;84(1):121–36. https://doi.org/10.1063/1.368009.
18. Bogaerts A, Gijbels R, Vlcek J. Modeling of glow discharge optical emission spectrometry: Calculation of the argon atomic optical emission spectrum. Spectrochim Acta B At Spectrosc. 1998;53(11):1517–26. https://doi.org/10.1016/s0584-8547(98)00139-6.
19. Iordanova S, Koleva I. Optical emission spectroscopy diagnostics of inductively-driven plasmas in argon gas at low pressures. Spectrochim Acta B Atomic Spectrosc. 2007;62(4):344–56. https://doi.org/10.1016/j.sab.2007.03.026.
20. Tian-Ye N, Jin-Xiang C, Lei L, Jin-Ying L, Yan W, Liang W, You L. A comparison among optical emission spectroscopic methods of determining electron temperature in low pressure argon plasmas. Chin Phys. 2007;16(9):2757–63. https://doi.org/10.1088/1009-1963/16/9/043.
21. Canal GP, Luna H, Galvão RMO, Castell R. An approach to a non-LTE Saha equation based on the Druyvesteyn energy distribution function: a comparison between the electron temperature obtained from OES and the Langmuir probe analysis. J Phys D Appl Phys. 2009;42(13):135202. https://doi.org/10.1088/0022-3727/42/13/135202.
22. Boffard JB, Lin CC, DeJosephJr CA. Application of excitation cross sections to optical plasma diagnostics. J Phys D Appl Phys. 2004;37(12):143–61. https://doi.org/10.1088/0022-3727/37/12/r01.
23. Boffard JB, Jung RO, Lin CC, Aneskavich LE, Wendt AE. Argon 420.1–419.8 nm emission line ratio for measuring plasma effective electron temperatures. J Phys D Appl Phys. 2012;45(4):045201. https://doi.org/10.1088/0022-3727/45/4/045201.
24. Boffard JB, Jung RO, Lin CC, Wendt AE. Optical emission measurements of electron energy distributions in low-pressure argon inductively coupled plasmas. Plasma Sources Sci Technol. 2010;19(6):065001. https://doi.org/10.1088/0963-0252/19/6/065001.
25. Zhu X-M, Chen W-C, Li J, Pu Y-K. Determining the electron temperature and the electron density by a simple collisional–radiative model of argon and xenon in low-pressure discharges. J Phys D Appl Phys. 2008;42(2):025203. https://doi.org/10.1088/0022-3727/42/2/025203.
26. Zhu X-M, Pu Y-K. Optical emission spectroscopy in low-temperature plasmas containing argon and nitrogen: determination of the electron temperature and density by the line-ratio method. J Phys D Appl Phys. 2010;43(40):403001. https://doi.org/10.1088/0022-3727/43/40/403001.
27. Zhu X-M, Pu Y-K, Celik Y, Siepa S, Schüngel E, Luggenhölscher D, Czarnetzki U. Possibilities of determining non-Maxwellian EEDFs from the OES line-ratios in low-pressure capacitive and inductive plasmas containing argon and krypton. Plasma Sources Sci Technol. 2012;21(2):024003. https://doi.org/10.1088/0963-0252/21/2/024003.
28. Siepa S, Danko S, Tsankov TV, Mussenbrock T, Czarnetzki U. On the OES line-ratio technique in argon and argon-containing plasmas. J Phys D Appl Phys. 2014;47(44):445201. https://doi.org/10.1088/0022-3727/47/44/445201.

29. Chiu Y, Austin BL, Williams S, Dressler RA, Karabadzhak GF. Passive optical diagnostic of Xe-propelled Hall thrusters. I, Emission cross sections. J Appl Phys. 2006;99(11):113304. https://doi.org/10.1063/1.2195018.
30. Karabadzhak GF, Chiu Y, Dressler RA. Passive optical diagnostic of Xe propelled Hall thrusters. II, Collisional-radiative model. J Appl Phys. 2006;99(11):113305. https://doi.org/10.1063/1.2195019.
31. Sommerville J, King L. An Optical Diagnostic for Xenon Hall Thrusters Including Metastable Contributions. In: 42nd AIAA/ASME/SAE/ASEE Joint Propulsion Conference & Exhibit. American Institute of Aeronautics and Astronautics; 2006. https://doi.org/10.2514/6.2006-4823.
32. Dressler RA, Chiu Y, Zatsarinny O, Bartschat K, Srivastava R, Sharma L. Near-infrared collisional radiative model for Xe plasma electrostatic thrusters: the role of metastable atoms. J Phys D Appl Phys. 2009;42(18):185203. https://doi.org/10.1088/0022-3727/42/18/185203.
33. Yang J, Yokota S, Kaneko R, Komurasaki K. Diagnosing on plasma plume from xenon Hall thruster with collisional-radiative model. Phys Plasmas. 2010;17(10):103504. https://doi.org/10.1063/1.3486530.
34. Wei L-Q, Li W-B, Ding Y-J, Zhu X-M, Wang Y-F, Hu J-F, Yan S-L, Yu D-R. A photographic method for in-orbit measurement of electron temperature distribution in the plume of Hall thrusters. Plasma Sources Sci Technol. 2018;27(8):084002. https://doi.org/10.1088/1361-6595/aad4cd.
35. Zhu X-M, Chen W-C, Pu Y-K. Gas temperature, electron density and electron temperature measurement in a microwave excited microplasma. J Phys D Appl Phys. 2008;41(10):105212. https://doi.org/10.1088/0022-3727/41/10/105212.
36. Zhu X-M, Wang Y-F, Wang Y, Yu D-R, Zatsarinny O, Bartschat K, Tsankov TV, Czarnetzki U. A xenon collisional-radiative model applicable to electric propulsion devices: II, Kinetics of the 6s, 6p, and 5d states of atoms and ions in Hall thrusters. Plasma Sources Sci Technol. 2019;28(10):105005. https://doi.org/10.1088/1361-6595/ab30b7.
37. Wang Y, Wang Y-F, Zhu X-M, Zatsarinny O, Bartschat K. A xenon collisional-radiative model applicable to electric propulsion devices: I, Calculations of electron-impact cross sections for xenon ions by the Dirac B-spline R-matrix method. Plasma Sources Sci Technol. 2019;28(10):105004. https://doi.org/10.1088/1361-6595/ab3125.
38. Priti, Gangwar RK, Srivastava R. Collisional-radiative model of xenon plasma with calculated electron-impact fine-structure excitation cross-sections. Plasma Sources Sci Technol. 2019;28(2):025003. https://doi.org/10.1088/1361-6595/aaf95f.
39. Holste K, Gärtner W, Zschätzsch D, Scharmann S, Köhler P, Dietz P, Klar PJ. Performance of an iodine-fueled radio-frequency ion-thruster. Eur Phys J D. 2018;72(1):. https://doi.org/10.1140/epjd/e2017-80498-5.
40. Dietz P, Gärtner W, Koch Q, Köhler PE, Teng Y, Schreiner PR, Holste K, Klar PJ. Molecular propellants for ion thrusters. Plasma Sources Sci Technol. 2019;28(8):084001. https://doi.org/10.1088/1361-6595/ab2c6c.
41. Saloman EB. Energy Levels and Observed Spectral Lines of Xenon, Xe I through Xe LIV. J Phys Chem Ref Data. 2004;33(3):765–921. https://doi.org/10.1063/1.1649348.
42. Johnson EO, Malter L. A Floating Double Probe Method for Measurements in Gas Discharges. Phys Rev. 1950;80(1):58–68. https://doi.org/10.1103/physrev.80.58.
43. Kramida A, Ralchenko Y. NIST Atomic Spectra Database, NIST Standard Reference Database 78: National Institute of Standards and Technology; 1999. https://doi.org/10.18434/T4W30F.
44. Izenman AJ. Linear Discriminant Analysis. In: Modern Multivariate Statistical Techniques. In: Springer Texts in Statistics. Springer; 2013. p. 237–80. https://doi.org/10.1007/978-0-387-78189-1_8.
45. Pauca VP, Piper J, Plemmons RJ. Nonnegative matrix factorization for spectral data analysis. Linear Algebra Appl. 2006;416(1):29–47. https://doi.org/10.1016/j.laa.2005.06.025.
46. Gorsuch RL. Factor Analysis: Psychology Press; 2013. https://doi.org/10.4324/9780203781098.
47. Boffard JB, Jung RO, Lin CC, Aneskavich LE, Wendt AE. Optical diagnostics for characterization of electron energy distributions: argon inductively coupled plasmas. Plasma Sources Sci Technol. 2011;20(5):055006. https://doi.org/10.1088/0963-0252/20/5/055006.

Publisher's Note